

Accepted for publication in The Astronomical Journal

## *HST/ACS Images of the GG Tauri Circumbinary Disk*

J.E. Krist<sup>1,2</sup>, K.R. Stapelfeldt<sup>1</sup>, D.A. Golimowski<sup>3</sup>, D.R. Ardila<sup>3</sup>, M. Clampin<sup>4</sup>, A.R. Martel<sup>3</sup>, H.C. Ford<sup>3</sup>, G.D. Illingworth<sup>5</sup>, G.F. Hartig<sup>2</sup>

### ABSTRACT

*Hubble Space Telescope* Advanced Camera for Surveys images of the young binary GG Tauri and its circumbinary disk in  $V$  and  $I$  bandpasses were obtained in 2002 and are the most detailed of this system to date. They confirm features previously seen in the disk including: a “gap” apparently caused by shadowing from circumstellar material; an asymmetrical distribution of light about the line of sight on the near edge of the disk; enhanced brightness along the near edge of the disk due to forward scattering; and a compact reflection nebula near the secondary star. New features are seen in the ACS images: two short filaments along the disk; localized but strong variations in the disk intensity (“gaplets”); and a “spur” or filament extending from the reflection nebulosity near the secondary. The back side of the disk is detected in the  $V$  band for the first time. The disk appears redder than the combined light from the stars, which may be explained by a varied distribution of grain sizes. The brightness asymmetries along the disk suggest that it is asymmetrically illuminated by the stars due to extinction by nonuniform circumstellar material or the illuminated surface of the disk is warped by tidal effects (or perhaps both). Localized, time-dependent brightness variations in the disk are also seen.

*Subject headings:* stars: circumstellar matter — stars: individual (GG Tauri) — stars: pre-main sequence — stars: binaries

---

<sup>1</sup>Jet Propulsion Laboratory, 4800 Oak Grove Dr., Pasadena, CA 91109.

<sup>2</sup>Space Telescope Science Institute, 3700 San Martin Dr., Baltimore, MD 21218.

<sup>3</sup>Department of Physics and Astronomy, Johns Hopkins University, 3400 North Charles Street, Baltimore, MD 21218.

<sup>4</sup>NASA Goddard Space Flight Center, Code 681, Greenbelt, MD 20771.

<sup>5</sup>UCO/Lick Observatory, University of California, Santa Cruz, CA 95064.

## 1. Introduction

Judging by population statistics in nearby star forming regions like the Taurus, Ophiuchus, and Chameleon molecular clouds (Duchêne 1999), the majority of young ( $<10$  Myr) stars in them belong to bound, multiple systems. Many, if not most, of these stars are surrounded by dusty envelopes or disks. Some circumstellar disks (disks around individual stars) in multiple systems have been studied from visible through radio wavelengths (*e.g.* HK Tau/c; Stapelfeldt et al. 1998). Because of tidal interactions with the other stars in their systems, these stars may have disks truncated at outer radii. Circumbinary disks, however, appear to be somewhat more rare, and only two, UY Aurigae (Close et al. 1998) and GG Tauri, have been studied thoroughly from optical to radio wavelengths.

GG Tau is a young, multiple system located in the Taurus star forming region, 140 pc distant. It includes two binaries, the brighter of which, GG Tau Aa/Ab (hereafter simply called GG Tau), is composed of two T Tauri stars separated by  $0''.25$ . The brighter star, GG Tau Aa, was given an M0 spectral classification by Hartigan & Kenyon (2003) and the fainter GG Tau Ab is type M2. This system is surrounded by a fairly massive ( $0.1 M_{\odot}$ ), optically-thick disk. Imaging at radio (Guilloteau, Dutrey, & Simon 1999), near-infrared (Silber et al. 2000; Roddier et al. 1996), and visible (Krist, Stapelfeldt, & Watson 2002) wavelengths has revealed that inside of 150 AU the disk has been largely cleared by tidal interactions with the binary. The dust near the inner edge is illuminated by the stars, creating the appearance of a narrow circumbinary ring inclined by  $\sim 37^{\circ}$  from face-on. Dust at larger radii may be shadowed by the inner material, so the disk is likely larger than it appears in scattered light.

The first adaptive optics (AO) images of GG Tau by Roddier et al. (1996; hereafter R96) showed the ring in reflected light in *JHK* bands. It appeared clumpy and had radial spokes that seemed to connect the ring to the stars. R96 suggested that these could be accretion streams, similar to those predicted by Artymowicz & Lubow (1996). These features, however, appeared nearly as bright as the optically thick disk, so they would have to be rather dense to reflect a sufficient amount of light to be detected.

*Hubble Space Telescope (HST)* imaging of GG Tau at visible wavelengths (Krist, Stapelfeldt, & Watson 2002, hereafter KSW02) using the WFPC2 camera and in the near-IR with NICMOS (Silber et al. 2000; McCabe, Duchêne, & Ghez 2002, hereafter MDG02) showed that the ring is generally smooth and lacks radial spokes, suggesting that those seen by R96 were instrumental artifacts. The *HST* images revealed brightness and structural asymmetries in the ring. For instance, there appears to be a “gap” in the ring that is likely a shadow caused by material between the ring and the stars. Also, the brightest section of the ring is not along the closest edge, as would be expected from forward scattering by dust grains in a uniformly illuminated, symmetrical disk, but is instead offset in azimuth by  $\sim 20^{\circ}$ . These

and other asymmetries suggest that the illuminated surface of the disk is warped and/or the illumination is shadowed by circumstellar material. The latter case is bolstered by a compact reflection nebulosity seen near the secondary star in the WFPC2 image. The *HST* studies also showed that the ring is redder than the combined observed light from the stars.

Because the ring is optically thick, the dust density distribution and grain properties cannot be directly derived from the reflected-light images. Three-dimensional, multiple-scattering models have been used to examine possible dust distributions and grain properties (Wood, Crosas, & Ghez 1999; Duchêne et al. 2004, hereafter D04) with constraints provided by both the scattered light and thermal emission images. The two important measurements provided by the visible and near-IR images are the ratio of the forward side to back side (F/B) brightnesses and the ratio of integrated ring flux to the combined stellar fluxes. The first ratio sets limits on the degree of forward scattering in the models, which is a function of particle size. The variation in forward scattering with wavelength can therefore place constraints on the assumed grain size distribution function. The second ratio can indicate the amount of light from the stars lost by multiple scattering or extinction by circumstellar material.

Until now, the only images of the GG Tau ring at visible wavelengths were those from the WFPC2 camera on *HST*. However, the F555W (WFPC2 *V* band) image was neither deep enough nor sufficiently free of point spread function (PSF) subtraction artifacts to unambiguously show the back side of the ring, and thus failed to provide a strong constraint on the variation of forward scattering with wavelength. To remedy this situation, images of GG Tau have been taken using the Advanced Camera for Surveys (ACS) on *HST*. Its finer pixel scale and more stable PSF allows better subtractions of the stellar glare, which are required to reveal the ring against the background glare from the stars.

## 2. Observations, Stellar Photometry, and PSF Subtraction

The GG Tau images were taken as part of the ACS Investigation Definition Team’s circumstellar disk program (*HST* program 9295) on 12 September 2002. The system was observed with the ACS High Resolution Camera (HRC), which has a pixel scale of  $\sim 0''.025$  pixel $^{-1}$  and a PSF FWHM of 50 mas in the *V* band. Identical sets of exposures were taken at two orientations with the telescope rolled about its optical axis by  $28^\circ$ . These rolls permit improved differentiation of PSF artifacts (which remain static as seen by the detector regardless of roll) from real disk structures (which change orientation with telescope roll). They also allow regions of the ring obscured by the diffraction spikes at one roll to be replaced by unobscured pixels from the other. At each roll, identical sets of short-to-long

duration exposures were taken through filters F555W (ACS *V* band) and F814W (ACS *I* band) (Table 1). The data were calibrated by the *HST* data archive. Duplicate exposures were combined with cosmic ray rejection and saturated pixels in long exposures were replaced by scaled values from shorter ones, providing high-dynamic-range images.

Because of the faintness of the GG Tau disk and its proximity to the stars, the stellar PSFs had to be subtracted using images of another star. HD 260655 (K7V) was chosen as a reference PSF because its color was similar to that of the brighter binary component, GG Tau Aa. It was observed in an orbit immediately following the GG Tau observations in order to reduce the influence of time-dependent focus changes that could lead to PSF mismatches and increased subtraction residuals. Short-to-long exposures were taken and processed in the same manner as the GG Tau images. Unfortunately, the short F814W image was slightly saturated.

## 2.1. PSF Fitting and Stellar Photometry

Because the separation between the binary components is small and portions of their PSFs overlap, simple aperture photometry may introduce unacceptable errors. To obtain accurate positions and flux measurements, simultaneous PSF fitting of both components was undertaken. For the F555W data, Tiny Tim model PSFs (Krist & Hook 2003) were matched to the observations, as they were in the WFPC2 study (KSW02). Iterative model-fitting phase retrieval analysis (Krist & Burrows 1995) was used to determine the aberration parameters (focus, coma, astigmatism) appropriate for the observations by measuring GG Tau Aa in the shortest exposure at the first orientation. These values were then used in Tiny Tim to generate subsampled, geometrically-distorted models with colors similar to the GG Tau stars. Within an iterative optimization routine the models were shifted via cubic convolution interpolation, rebinned to normal pixel sampling, convolved with a kernel representing blurring from HRC CCD charge diffusion, and then scaled in intensity to match the binary components. The *HST* images were not corrected at this point for geometric distortion to avoid potential errors caused by interpolation.

PSF fitting photometry in F814W was more complicated because the HRC CCD suffers from a “red halo” (Sirriani et al. 1998). This appears as a diffuse, smooth halo of light that can be seen extending out to  $\sim 4''$  from the stars in the deep F814W exposures. Its surface brightness decreases with increasing radius. It is caused by red photons that pass completely through the CCD and are scattered to large angles within the glass mounting substrate and then back into the detector. The halo begins to appear between 6000–7000Å and by 10000Å it can contain more than 30% of the stellar flux. It is seen in the unsubtracted F814W image

Table 1. ACS GG Tau and Reference PSF Exposures

Star	Filter	Exposure
GG Tau <sup>1</sup>	F555W	2 x 3s
		2 x 30s
		2 x 1275s
	F814W	2 x 1s
		1 x 10s
		2 x 25s
		2 x 250s
	HD 260655	2 x 0.2s
		2 x 0.8s
		2 x 2s
		2 x 10s
		2 x 50s
		3 x 300s
		2 x 2s
		2 x 50s
		2 x 200s
		3 x 830s

<sup>1</sup>The listed GG Tau exposures were duplicated after rolling the telescope 28°.

in Figure 1, where it washes out the diffraction structure in the wings. The effect is sensitive to the color of the object over a broad passband, leading to potential mismatches between target and reference PSFs, even for similar spectral types.

At this time, Tiny Tim does not model the red halo with sufficient accuracy to provide good subtractions. Rather than fitting the F814W GG Tau binary with PSF models we instead used an image of HD 17637 that was observed in an *HST* calibration program (we could not use HD 260655 as it was saturated in this filter). HD 17637 is a K5V star, so it is slightly more blue than GG Tau Aa. However, it should be a better match than a Tiny Tim model. The PSF image, which was not corrected for geometric distortion, was interpolated to  $5\times$  finer sampling (the observed HRC PSF is oversampled by a factor of 1.4 at  $\lambda = 8000\text{\AA}$  relative to Nyquist sampling). It was then used by the same PSF fitting routine described previously (excluding charge diffusion blurring, which the observed reference PSF already contained). The fluxes were aperture corrected. Because the stellar photometry was obtained in the distorted images, adjustments to the fluxes were required to account for the difference between the pixel area assumed in the calibrated data and the true area (this is described in the ACS Data Handbook; Pavlovsky et al. 2004). The average fluxes of the measurements at each roll were converted to standard  $V$  and  $I_c$  magnitudes (Table 2) using the SYNPHOT synthetic photometry package. An M1.5V spectrum was assumed for both components of GG Tau A. The estimated photometric errors are  $\pm 0.03$  mag.

The positions of the binary components were corrected for geometric distortion, and the resulting orientations were converted to position angles based on the telescope orientations provided in the image file headers. The mean separations are  $0''.251$  (F555W) and  $0''.250$  (F814W), with errors of  $\pm 0''.002$ . The mean position angles are  $346.3^\circ$  (F555W) and  $345.9^\circ$  (F814W), with errors of  $\pm 0.5^\circ$ .

The flux of the ACS reference star, HD 260655, was also measured in each filter to derive the normalization factors for PSF subtractions. The F555W flux was obtained by fitting the Tiny Tim PSF. As with GG Tau, the fit in F814W was done using HD 17637. HD 260655 was saturated in the core in F814W, and those pixels were given zero weight in the fit. As with GG Tau, the fluxes were converted to standard magnitudes assuming a M1.5V spectrum. The estimated errors are  $\pm 0.03$  mag (F555W) and  $\pm 0.06$  mag (F814W).

Besides GG Tau A, other stars are seen in the HRC field and were measured using  $r = 0''.4$  apertures in the distortion-corrected images. The stars' photometry and positions relative to GG Tau A are given in Table 2. The fluxes were aperture corrected and converted to standard magnitudes assuming a M5.5V spectrum for the GG Tau B components and a K5V spectrum for the others. The estimated photometric errors are  $\pm 0.05$  for GG Tau B and  $\pm 0.09$  for the others. The GG Tau B binary has a separation of  $\sim 1''.5$ . The fainter

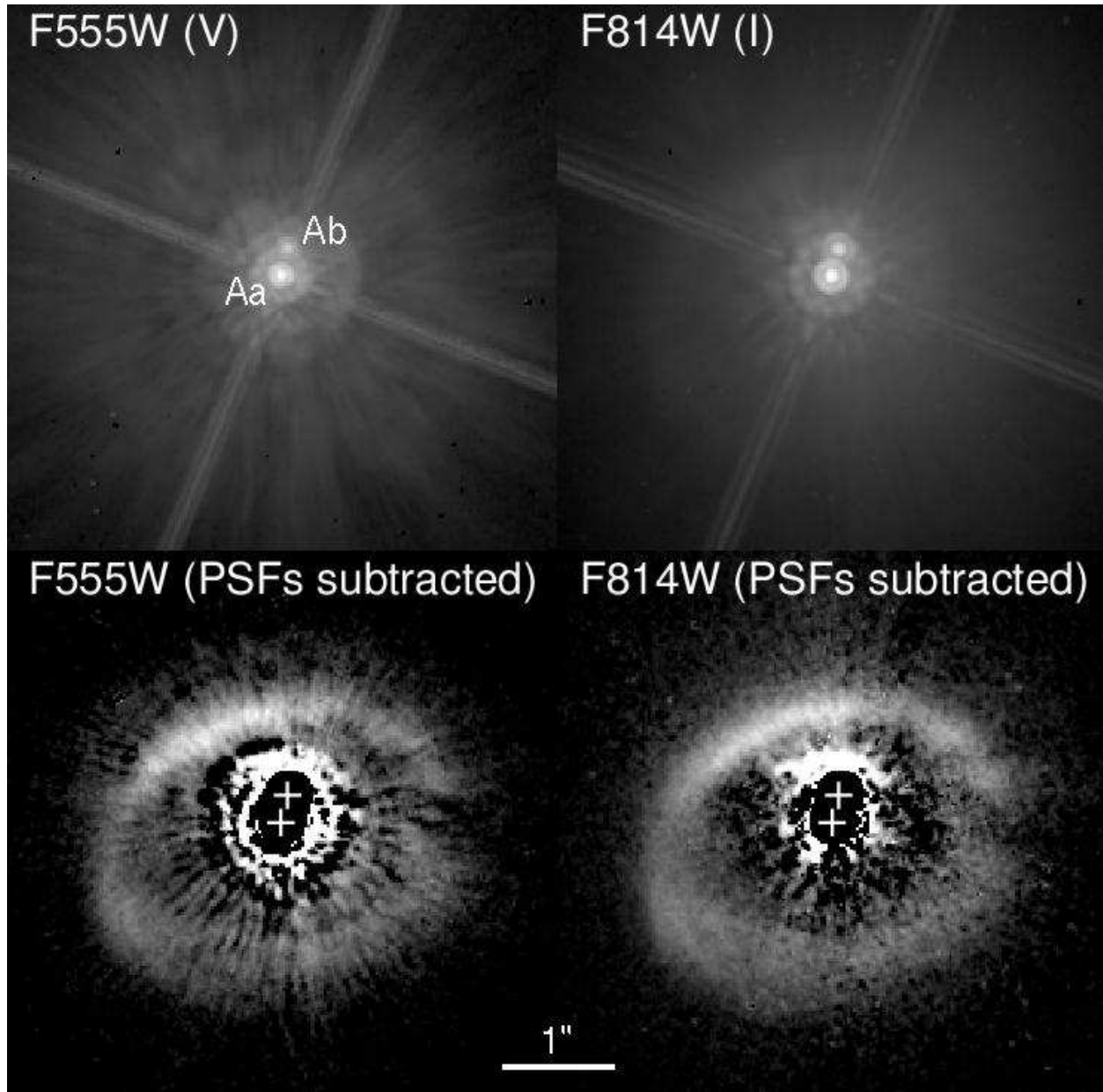


Fig. 1.— ACS images of GG Tau. (Top) Unsubtracted images in filters F555W (*V*) and F814W (*I*), displayed with logarithmic stretches. (Bottom) Combined first and second orientation images after subtraction of reference PSFs, displayed with square-root stretches. The locations of the binary components are marked with crosses. North is up in all of these images.

component, Bb, is very red ( $V - I_c = 4.55$ ) and was assigned a spectral type of M7 by White et al. (1999). The brighter star, Ba, was given an M5 type. Designations for the other stars in the field have not been made in previous studies, so we assign them arbitrary names. The colors of these stars imply that they are of types earlier than M2. One of them, which we designate GG Tau 1, was first noted by Silber et al. (2000), and further observations by Itoh et al. (2002) indicated that its motion relative to GG Tau A is consistent with it being a background star.

For comparison with the 1997 WFPC2 observations (KSW02) and the new ACS ones, the 1994 WFPC2 F555W and F814W images of GG Tau Aa/Ab (Ghez et al. 1997) were also measured by fitting Tiny Tim PSF models using the KSW02 routines. These measurements are independent of those reported by Ghez et al. (who fitted observed PSFs rather than models), which were later converted to standard magnitudes by White & Ghez (2001). Our values for these images for Aa & Ab are  $V = 12.34 \pm 0.03$  &  $15.31 \pm 0.06$  and  $I_c = 10.50 \pm 0.03$  &  $12.28 \pm 0.04$ . These are about 0.05 mag (Aa) and 0.1 mag (Ab) fainter than the values reported by White & Ghez (2001), due either to the differences in measurement techniques or assumptions for spectral types used when converting to the standard magnitude system. For consistency, we use only our photometric measurements and those of KSW02. There were no differences between our measurements of the position angle and separation and those reported by Ghez et al. (1997). Comparison of the mean of the F555W and F814W ACS position angles to the 1994 angle provides an average binary angular motion of  $-1.52^\circ \text{ yr}^{-1} \pm 0.1^\circ$ . There is no significant change in separation between the two epochs.

## 2.2. PSF Subtraction

Using the measured photometry and positions, synthetic binaries for each filter at each orientation were constructed by shifting and intensity-scaling the HD 260655 images. These images were subtracted from GG Tau, and the resulting images were then corrected for geometric distortion. The data for each filter from both rolls were combined by rotating the image from the second roll to match the first, replacing pixels within the diffraction spikes at one roll with those from the other, and then averaging the two. The results are shown in Figure 1. Because of the larger mismatch in color between the GG Tau stars and HD 260655 within the F555W passband, the subtraction residuals (radiating streaks and rings around the stars) are greater in that filter than in F814W.

An initial review of the F814W images revealed significant contamination by residuals caused by the incomplete subtraction of the red halo (Figures 2a,2b). This remnant halo may be caused by the color mismatch between GG Tau Ab ( $V - I_c = 2.79$ ) and the reference

Table 2. GG Tauri System Stellar Photometry

Star	<i>V</i>	<i>I<sub>c</sub></i>	<i>V</i> – <i>I<sub>c</sub></i>	Sep <sup>a</sup>	P.A. <sup>b</sup>
GG Tau Aa	12.23	10.43	1.80		
GG Tau Ab	15.18	12.37	2.81		
GG Tau Ba	17.11	13.41	3.70	10''.2	185.6°
GG Tau Bb	19.94	15.39	4.55	11''.2	179.8°
GG Tau 1	21.55	19.28	2.27	6''.2	241.1°
GG Tau 2	16.90	16.14	0.76	13''.5	211.5°
GG Tau 3	25.4	22.6	2.8	11''.6	7.9°
GG Tau 4	16.95	16.24	0.71	16''.7	45.9°
GG Tau 5	22.45	20.27	2.19	16''.7	42.2°
HD 260655	9.53	7.86	1.67		

<sup>a</sup>Distance measured from GG Tau A binary midpoint

<sup>b</sup>Position angle measured from GG Tau A binary midpoint

PSF ( $V - I_c = 1.77$ ). However, given that GG Tau Aa is  $\sim 6 \times$  brighter than Ab, it may more likely be the result of small differences between the spectra of Aa and HD 260655 within the F814W passband, despite their nearly equal  $V - I_c$  colors.

When the F814W PSF-subtracted, distortion-corrected images of GG Tau from each roll are rotated to a common sky orientation and the second is subtracted from the first, an asymmetry in the halo becomes apparent (Figure 2d). It is clearly instrumental because the residuals are not confined to the ring. Some of the asymmetry is caused by the distortion correction combined with the different rolls. The HRC detector is tilted relative to the incident beam to minimize focus variations over the field, resulting in significant geometric distortion (for instance, the diffraction spikes are  $7^\circ$  from being perpendicular in the uncorrected images). Assuming the halo is circularly symmetric in detector coordinates, then after distortion correction it will appear elliptical with the major axis roughly along the (+X,+Y) diagonal. When the second image is rotated to match the sky orientation of the first, the angle of the residual halo axis will be different between the two images (compare 2a and 2b). If the halo was perfectly symmetric on the detector, then the residuals should be symmetric as well, but they are not, suggesting some intrinsic asymmetry. Given that the detector is tilted relative to the incoming beam, the halo may be brighter on one side than the other due to a preferential scattering angle within the mounting substrate. The halo may also be field-dependent due to changes in the incident beam angle.

In regions where the halo effect is strong, we estimate that the portion of the subtraction residuals caused by halo mismatches correspond to  $\sim 15\%$  the brightness of the disk.

### 3. Results

#### 3.1. General Features

The PSF-subtracted ACS images provide the clearest views of the GG Tau disk obtained so far in scattered light. The use of two rolls provides complete images of the ring and avoids diffraction spike residuals seen in the previous single-roll WFPC2 and NICMOS images. Excluding the red halo problem, the relatively field-independent ACS PSF provides somewhat better subtractions than are possible with WFPC2, resulting in higher contrast views of the disk structure (Figure 3). The finer resolution also permits better registration of the PSFs with reduced interpolation artifacts. In addition, the deeper exposures allow the far, southern side of the ring to be unambiguously imaged in  $V$  for the first time.

In general, the system looks much as it did in the WFPC2 and NICMOS images, though more subtle intensity variations are visible. The outer apparent edge measures  $3.^{\prime\prime}7$  by  $3.^{\prime\prime}0$ .

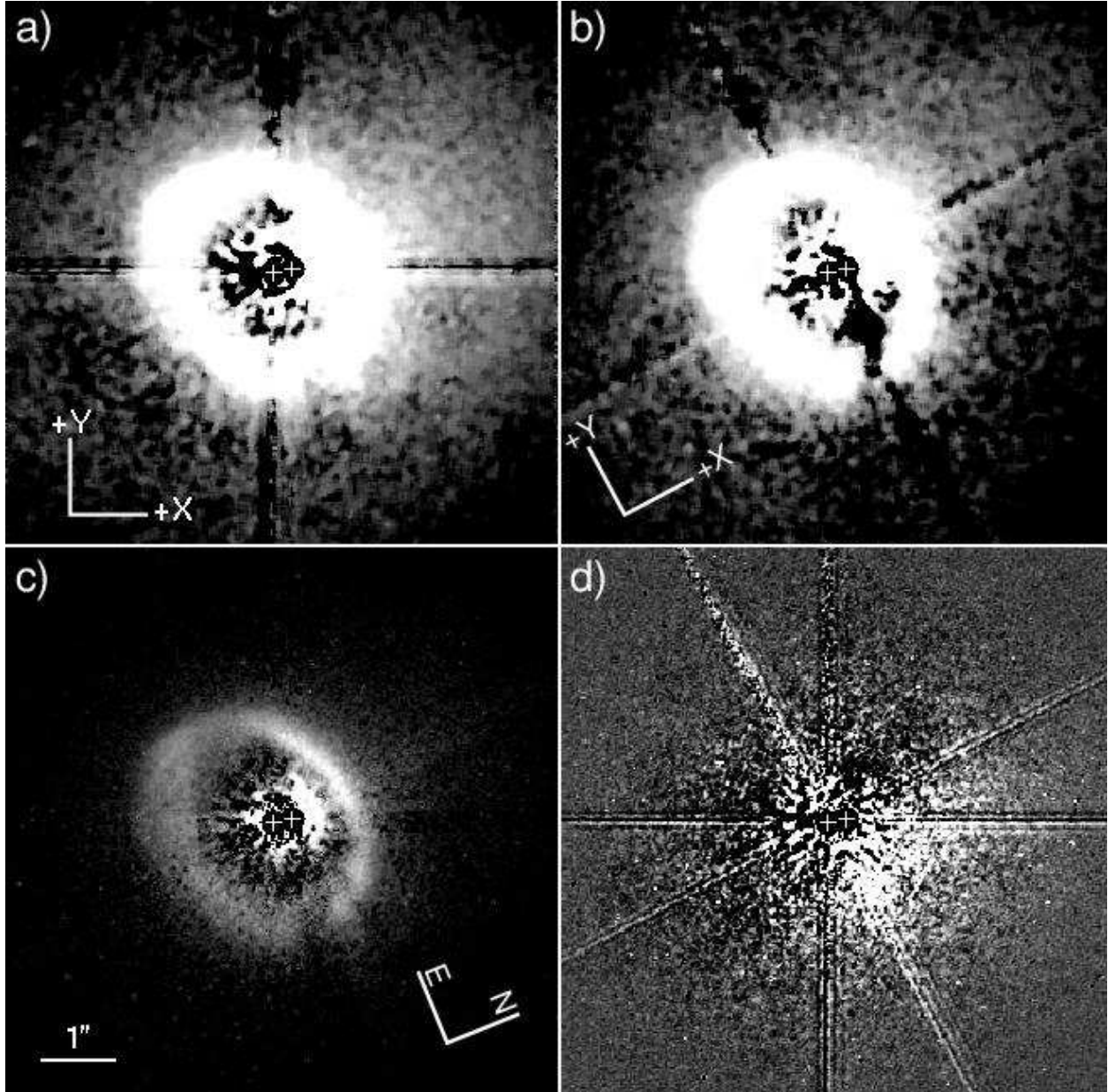


Fig. 2.— ACS F814W ( $I$ ) images of GG Tauri demonstrating the impact of the red halo. (a) PSF-subtracted image from the first orientation with an intensity stretch chosen to highlight the residual halo, which can be seen outside of the ring. The halo is brighter towards the upper right. (b) The image from the second orientation. Note that the asymmetry in the halo is fixed with respect to the detector axes (indicated by the +X,+Y compass). (c) Square-root stretch of the combined F814W images, for reference. (d) The subtraction of the second F814W PSF-subtracted image from the first, showing the instrumental halo asymmetry (linear stretch). All of the images are at the same orientation.

The northern side is peak is  $\sim 3.3 \times$  brighter than the southern. This is expected from forward scattering by dust grains, as the northern side is closer to us as determined from the measured rotation of the disk and the motion of the binary (Guilloteau, Dutrey, & Simon 1999). It has maximum surface brightnesses of  $V \approx 18.4$  and  $I_c \approx 15.9$  mag arcsec $^{-2}$ . The southern, more distant side of the ring appears about twice as thick as the nearer one. This is a projection effect, as both the inner wall and upper surface of the backside of the disk are seen there while in the north only the illuminated upper surface is visible (see Figure 2 in Silber et al. 2000). The west side appears thinner, brighter, and more irregular than the east side. The inner edge of the ring is fairly well defined in the north but is diffuse to the east and south, and along the west it is highly irregular. The outer edge is fairly smooth except in the west. Because the disk is optically and geometrically thick, its inclination causes the midpoint between the stars to appear offset  $\sim 0''.25$  forward from the ring center (as defined by the center of the ellipse fit to a trace through the ring peak azimuthal isophotes).

The images clearly show the  $0''.4$  wide “gap” in the western section of the ring between PA=254° – 275° that was identified in previous studies (Figure 3). Within it the surface brightness decreases by one-half relative to the adjacent sections of the ring. In  $V$  a PSF subtraction residual passes through the middle of the gap. There are other, less prominent “gaplets” along the northwest section centered at PA≈ 290° and 320°. There are two thin filaments along the outer edge of the ring between PA=100° – 150° in a section previously called the “kink” (Silber et al. 2000). They overlap with a separation of  $0''.11$  and are seen in both  $V$  and  $I$  bands as well as in the WFPC2  $I$  band image. They are not resolved in the NICMOS images. The filaments are better defined in  $V$  than  $I$ , perhaps due to the higher resolution or an increase in the opacity at shorter wavelengths in the dust lane separating them.

There is a “depression” in the surface brightness along the eastern interior edge (PA=90° – 114°) relative to the adjacent sections of the ring. The depression seems more defined in  $V$  than  $I$ , hinting of a possible increase in extinction at shorter wavelengths by circumstellar material. However, the red halo residuals prevent any definitive conclusions.

The interior of the ring does not appear to be completely clear, and it is brighter than the surrounding region immediately outside of the ring. This is especially apparent in the  $V$  image, which is free of any red halo contamination. Excluding any small regions with significant subtraction residuals near the stars that could bias the flux measurements, the interior has median surface brightnesses of  $V = 20.1 \pm 0.4$  and  $I_c = 18.1 \pm 0.4$  mag arcsec $^{-2}$ . Increasing the reference PSF intensity by 10% during PSF subtraction would eliminate this flux, but would lead to significant oversubtraction outside of the ring. This amount of adjustment is also greater than the photometric measurement errors allow.

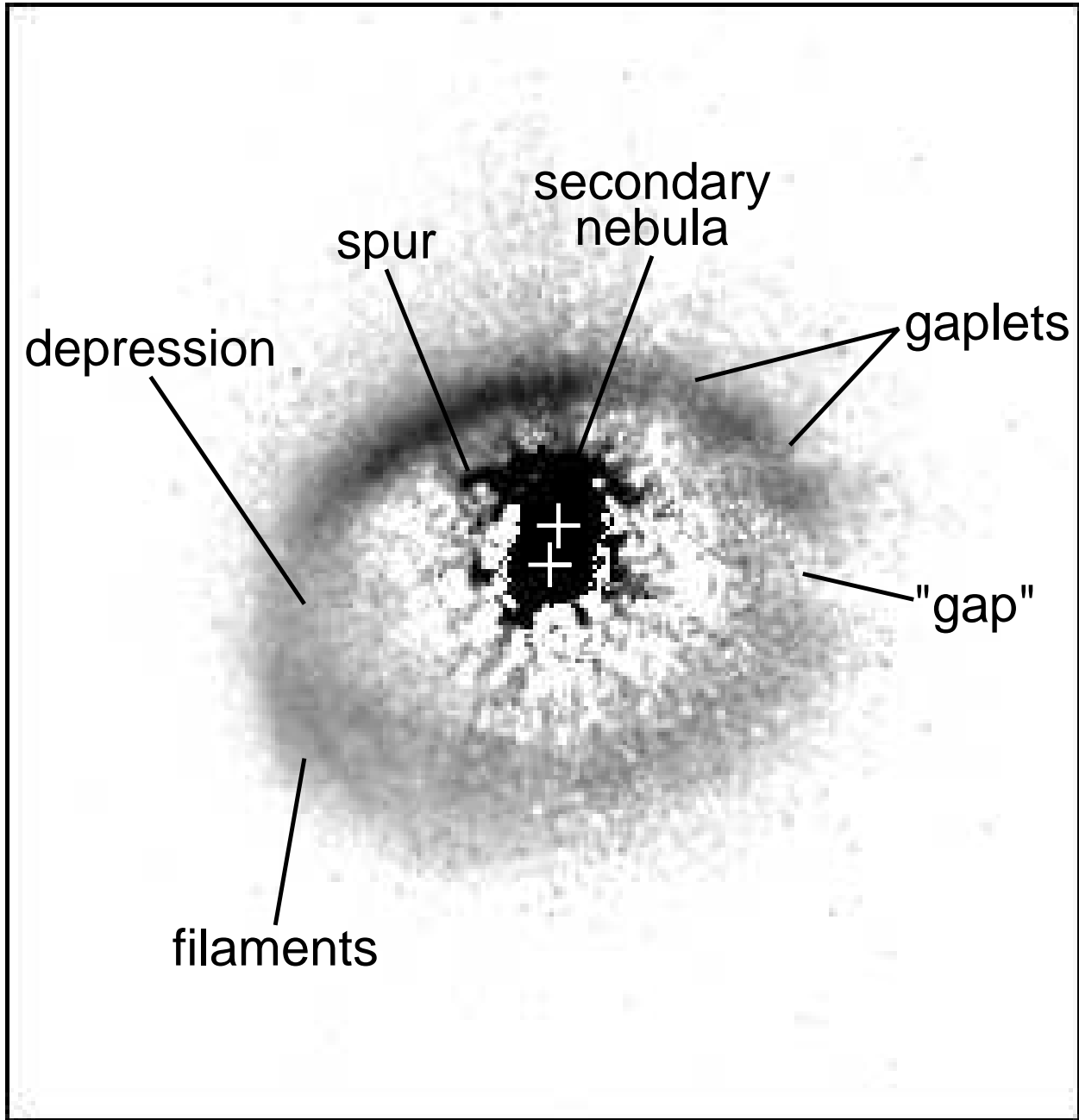


Fig. 3.— ACS F814W PSF-subtracted image of GG Tau with features identified (North is up).

As noted by KSW02 from the WFPC2 images, there appears to be a compact region of reflecting material adjacent to the secondary star on its north side. This “secondary arc” is clearly seen at the same position angle at both telescope orientations in  $I$ , and at nearly the same position in both  $V$  orientations. The greater subtraction residuals at  $V$  interfere with detail near the stars. It therefore appears to be real and is not an instrumental artifact. It extends out to  $\sim 0''.5$  from GG Tau Ab. Its shape and brightness are difficult to accurately determine given its proximity to the star. At  $0''.3$  from GG Tau Ab, its mean  $I$  band surface brightness is  $15.5 \pm 0.2$  mag arcsec $^{-2}$ . This apparent nebulosity can also be seen in the NICMOS images of Silber et al. (2000), though it was not identified or discussed there. In the NICMOS images of MDG02 it is located within the region of the diffraction spikes and is not seen. A short “spur” seems to extend from the nebulosity and runs parallel to the forward edge. This feature is seen at both orientations at  $I$ , though it is more prominent at the second roll. PSF subtraction artifacts interfere with its detection at  $V$ . There is no sign of it in the WFPC2 images, but the NICMOS image of Silber et al. (2000) does appear to show a similar feature in the same region. This spur therefore seems to be real and is probably not a PSF subtraction artifact. The brightness of the secondary nebula suggests that it is optically thick. As discussed in KSW02, it is too large to be a disk around the secondary and is too far from the star to be material trapped at the system’s Lagragian L2 point. Its nature is still unexplained. Its brightness and size makes it a good target for adaptive optics observations on future very large telescopes. Perhaps with additional resolution it will be possible to detect features such as spiral arms that could point to a dynamical cause for its existence.

### 3.2. Ring Photometry

Azimuthal surface brightness plots for the combined ACS data for each filter are shown in Figure 4, along with the WFPC2  $I$  band plot. The tracer line used for these was defined by the peaks of 3<sup>rd</sup>-order polynomials that were fit to the radial profiles extracted from the ACS  $I$  band image. The tracer was manually adjusted to cross the “gap”, where the fits failed to converge. The brightness at each azimuth was measured using the median flux within a  $0''.075^2$  box centered on line. An ellipse fit through the tracer has a semi-major axis of  $1''.47$ , minor axis position angle of  $20^\circ$ , and eccentricity of 0.63. These values agree well with those derived by MDG02 using a similar method.

Separate profiles (Figures 5 and 6) were extracted from the ACS images in each filter and at each orientation to quantify the variations caused by PSF subtraction errors, including the red halo asymmetry. The  $V$  band plots show a  $\sim 15\%$  difference along the forward edge

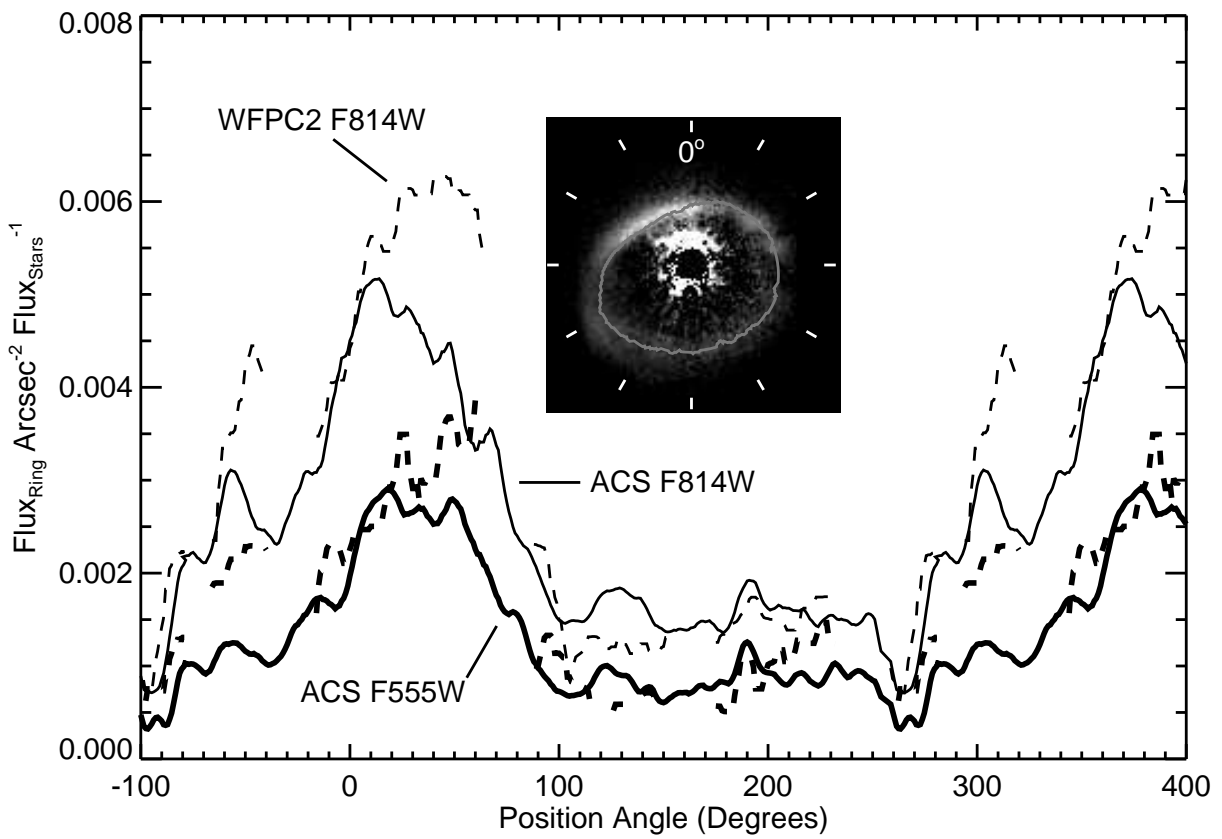


Fig. 4.— Azimuthal surface brightness profiles of the GG Tau ring as measured in the ACS and WFPC2  $V$  and  $I$  images. The data from the ACS roll- combined images are shown. The bold dashed line is WFPC2  $V$ . The values were measured along the line traced along the ring as shown in the inset image.

between the two orientations, which appears to be caused by subtraction residuals, but the other sections match to better than a few percent. The effects of the red halo asymmetry are apparent in the  $I$  band plots. They show that in the northwest quadrant ( $PA=250^\circ - 350^\circ$ ) the ring surface brightness was  $20\% - 60\%$  greater at the first roll than the second. The ring is otherwise  $10\% - 20\%$  brighter in the second-roll image in the north ( $PA=10^\circ - 70^\circ$ ) and the south-southeast ( $PA=110^\circ - 180^\circ$ ). The brightnesses are similar in the southwest quadrant and in the eastern apex.

To allow quantitative comparisons with the D04 WFPC2 and NICMOS results, fluxes in the ACS  $V$ , ACS  $I$ , and WFPC2  $I$  images were measured with the same elliptical annular aperture that they used. The concentric ellipses defining the annulus had semi-major axes of  $0''.99$  and  $2''.2$ ,  $e = 0.65$ , minor axis  $PA=20^\circ$ , and were concentric with the ellipse fit through the tracer line. Fluxes were measured separately in the forward ( $PA=275^\circ - 95^\circ$ ) and back ( $PA=95^\circ - 275^\circ$ ) halves of the annulus.

To exclude any contribution from the “secondary arc”, that region was manually masked out within the aperture. The same area was essentially masked by the diffraction spikes in the NICMOS images measured by MDG02 (and used by D04 and so did not contribute to their values. However, their measurement of the WFPC2 image may be biased by it.

To estimate the photometric errors introduced by the red halo asymmetry, modified ACS  $I$  band images were constructed for each roll. Pixels containing diffraction spikes at one roll were replaced by the corresponding, uncontaminated pixels from the other roll. This provided two separate images of the entire ring. Replacing the diffraction spikes with data from the other roll should not greatly impact the photometry as the spikes cover a small total area of the ring. The same procedure was applied to the two  $V$  images as well. The ring fluxes from these separate images were used to define the error ranges in the flux ratios that follow. In addition, for the purposes of the flux ratio measurements only, the diffraction spike regions in the WFPC2  $I$  image were replaced with the corresponding values from the roll-combined ACS  $I$  image.

The fluxes of the ring ( $F_{ring}$ ) relative to the combined stellar fluxes ( $F_{stars}$ ) are  $0.58\% \pm 0.01\%$  ( $V$ ) and  $1.09\% \pm 0.03\%$  ( $I$ ). The  $I$  band value likely represents the upper limit as the residual red halo would make the ring appear brighter than it actually is. The integrated forward/backside (F/B) flux ratios are  $1.25 \pm 0.01$  ( $V$ ) and  $1.31 \pm 0.10$  ( $I$ ). This measurement is clearly sensitive to the halo asymmetry. The WFPC2  $I$  band image values are  $F/B = 1.56 \pm 0.03$  and  $F_{ring}/F_{stars} = 1.23\% \pm 0.02\%$ . These can be compared to the measurements of the same WFPC2 image by D04, who derived  $F/B = 1.80 \pm 0.03$  and  $F_{ring}/F_{stars} = 1.30\% \pm 0.03\%$ . These larger values may be due to contamination by the secondary arc, which we avoided.

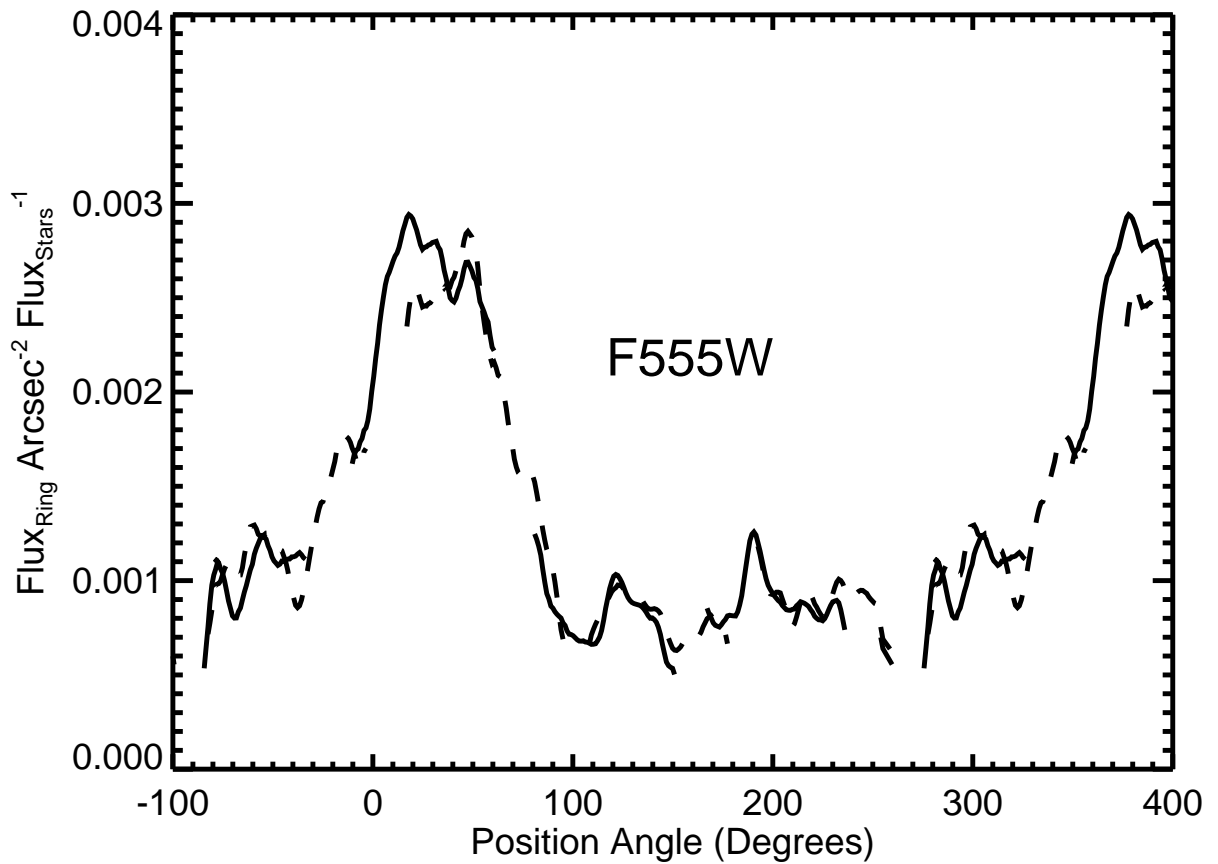


Fig. 5.— Azimuthal surface brightness profiles of the GG Tau ring measured in the ACS  $V$  image from each orientation (first orientation = solid, second = dashed). Regions contaminated by diffraction spike residuals are not plotted.

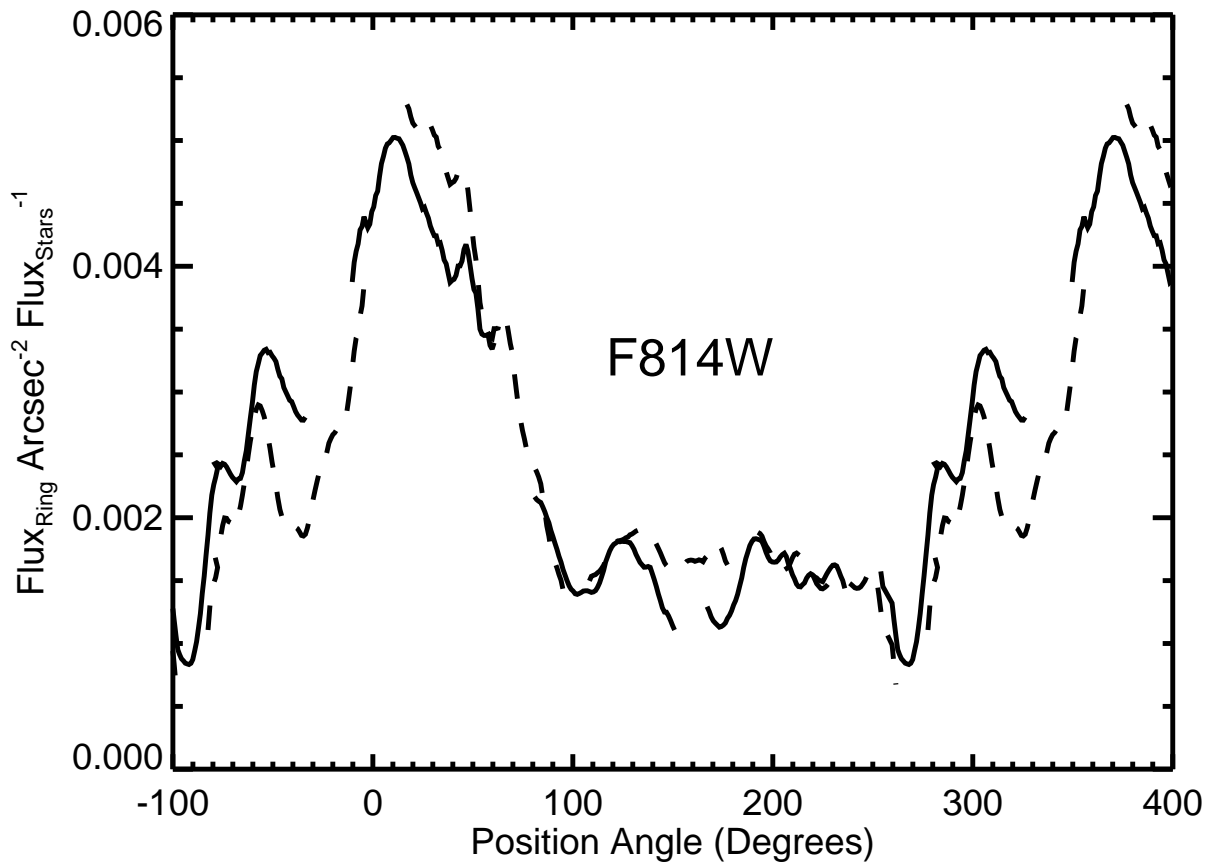


Fig. 6.— Azimuthal surface brightness profiles of the GG Tau ring measured in the ACS *I* image from each orientation (first orientation = solid, second = dashed). Regions contaminated by diffraction spike residuals are not plotted.

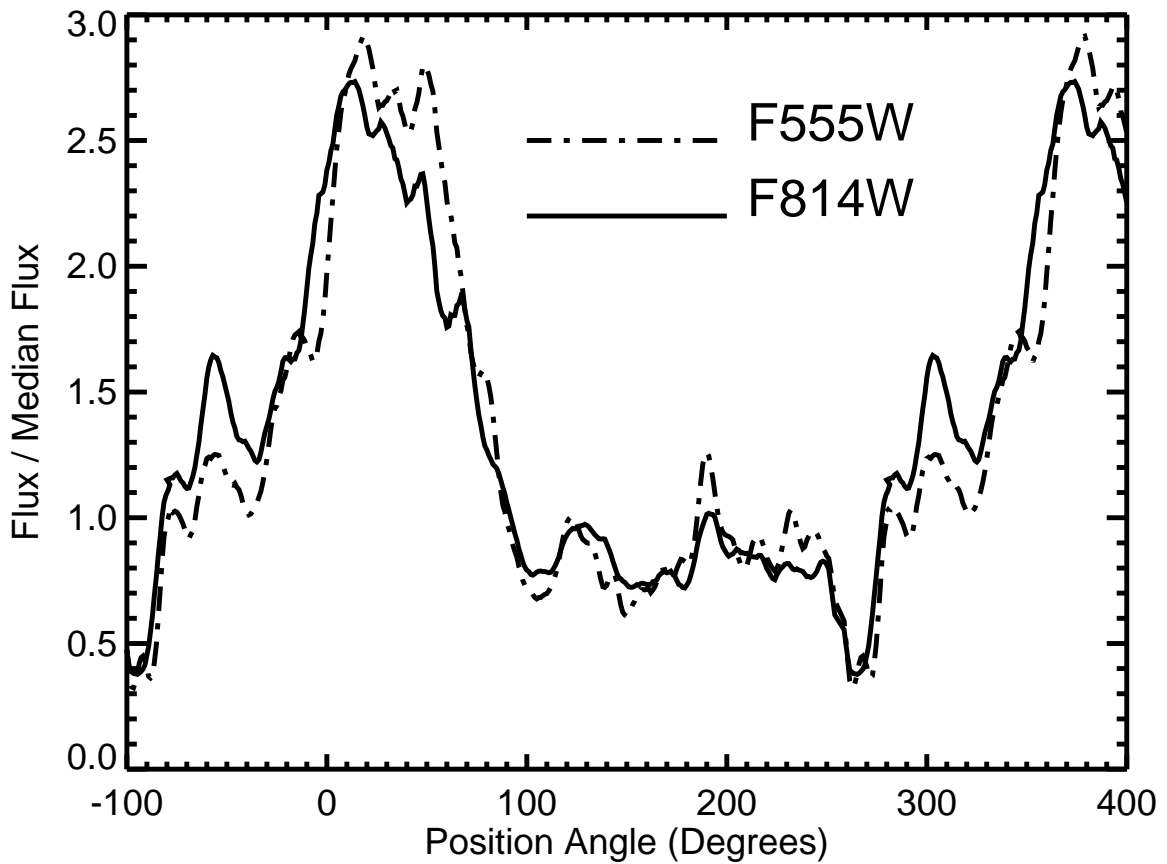


Fig. 7.— Azimuthal surface brightness profiles of the GG Tau ring measured in the roll-combined ACS  $V$  and  $I$  images, normalized by the median flux within the ring in each bandpass.

The ring is clearly redder in the visible than the measured light from the stars, with a median color of  $V - I_c = 2.66$  compared to 1.85 for the combined stellar fluxes. This agrees with the WFPC2 color measurement of  $V - I_c = 2.7$  (KSW02). We were unable to identify color variations along the ring that were above the uncertainty levels set by the red halo residuals. The data does suggest that the “depression” in the east is slightly more pronounced in  $V$  than  $I$ , but again that may be due to the residual red halo contributing to the addition  $I$  band flux.

#### 4. Discussion

The red halo contamination of the ACS F814W images prevents reliable detections of any low-level color variations within the ring. Given the photometric uncertainties, we limit our study to previously-seen and new structures, the general color of the ring in the visible, and the apparent difference in the forward edge brightness in the ACS and WFPC2  $I$  band images.

##### 4.1. The stars

The 1994 and 1997 WFPC2 and 2002 ACS data provide a limited sample of resolved visible-wavelength stellar photometry. Among these epochs GG Tau Ab varied by  $\Delta V = 0.61$  and  $\Delta I = 0.39$  while Aa changed by  $\Delta V = 0.11$  and  $\Delta I = 0.07$ . Ab also had a larger variation in color ( $\Delta V - I_c = 0.31$  versus 0.06 for Aa). Ab was most blue when it was brightest in  $V$ . This may be expected if the greater flux was due to increased accretion or an accretion spot coming into view due to stellar rotation (prominent accretion emission lines are seen in the  $V$  filter). This would suggest (ignoring the small sample) that Ab is the more active star. However, visible-wavelength *HST* spectra of the system (Hartigan & Kenyon 2003) indicate the opposite, unless the spectra were taken while Ab was in a quiescent state or when an accretion spot was not visible. Variation caused by the orbital motion of circumstellar material is a less likely explanation as Ab is not faintest in  $V$  and  $I$  at the same time.

The ACS angle and separation are the same (within the errors) as those reported by D04, whose well-resolved data were taken three months later. The PA errors for both measurements are larger than the  $0.38^\circ$  motion that would be expected between those epochs. The *HST* and D04 results indicate that the binary separation has not changed between 1994 – 2002 within the measurement errors, with a mean of  $0''.251 \pm 0''.003$ . Tamazian et al.

(2002) predicted a separation of  $0''.244$  for the epoch of the ACS observations, outside of the ACS measurement errors. Their predicted position angle is consistent with that observed, however. Their orbit may be biased by speckle results, which appear to show large and inconsistent variations in both PA and separation among the various epochs.

## 4.2. Comparisons with Similar Wavelengths

Comparisons of the ACS and WFPC2  $V$  band images do not reveal significant differences given the large PSF subtraction residuals and low exposure depth of the WFPC2 data. The general appearance is similar, but details such as the “depression” are poorly defined.

The ACS and WFPC2  $I$  band images are more comparable, though care must be taken to identify possible red halo effects. The general appearance is the same between them. The “gap” and secondary arc are both present, though the “gaplets” are not clearly present in the WFPC2 image (saturated column bleeding and diffraction spike residuals are present in the WFPC2 data). The “depression” is seen in the WFPC2 image, but it is not quite as well defined as it is in the ACS one.

The forward side does appear to be  $\sim 20\%$  brighter in WFPC2 than in ACS while the back sides are fairly equal. The integrated F/B ratios are 1.56 (WFPC2) and 1.31 (ACS), and the F/B amplitude ratios are  $\sim 4$  (WFPC2) and  $\sim 3.3$  (ACS). These discrepancies are above the uncertainty level expected from the red halo contamination in the ACS images. The back side of the ring has essentially the same brightness in both ACS and WFPC2 images. We believe that this is a real effect and indicates that some variability in the illumination pattern is likely. We note that there does not appear to be any significant changes in the positions of any features between the epochs, including the “gap”, indicating that any shadowing material causing it must be further from the stars than whatever is altering the pattern on the forward side.

Time-dependent variations in the appearances of reflection nebulae (envelopes, disks) surrounding young stars have been seen in R Mon (Lightfoot 1989), HH 30 (Stapelfeldt et al. 1999), and others. The timescale of these changes (*e.g.* 5 years for GG Tau) is too short to be caused by physical variations in the ring itself – they must be due to irregular illumination by the stars. Continuum emission from accretion spots on the star could increase the amount of light seen by a particular section of the disk, and as the star rotates they could vary the illumination pattern. Another possibility is shadowing from irregularly distributed circumstellar material near enough to the star to have a short orbital period or be placed where the orbital motion of the stars alters the projected light. The variation in

the brightness of the near edge between the two epochs matches the change in the observed flux from GG Tau Ab. This suggests that if light from Aa was blocked by a circumstellar disk in the ring plane, Ab could be the primary illumination source for this edge. A final potential cause is a light echo from an intense, short-term brightening of one of the stars. Due to the light travel time, the starlight reflected by the back side of the ring is seen about 1.3 days later than that from the forward edge. Differences in the phases of the stellar light curves might then result in equal backside ring brightnesses at both epochs while the forward side appears brighter at one of them. This would require either star to vary by more than twice its observed intensity range over a one day timescale.

#### 4.3. Comparisons with Different Wavelengths

As noted before, direct comparisons of the  $V$  and  $I$  ACS images are difficult because of the PSF subtraction residuals in  $V$  and the red halo in  $I$ . The profiles in Figure 7 would suggest that the forward edge in  $V$  is somewhat brighter than in  $I$ , relative to the rest of the ring. However, this difference is within the range of errors expected from the residuals.

The NICMOS image of Silber et al. (2000) appears very similar to those from ACS. The “gap” is clearly seen but not the “gaplets.” The “depression” in the east is also apparent, but the outer edge there is brighter compared to the ACS images. Silber et al. report a  $\sim 4.0 \times$  difference between the front and back side surface brightnesses, compared with  $\sim 3.3 \times$  seen in the ACS image. They note the presence of two compact features within the clear region that they suggest may be reflecting material. The first is an elongated streak to the southeast of the star. A similar feature is not seen in the other images, except perhaps in the MDG02  $J$  one, in which a thin residual streak extends along the same direction. However, this streak appears sharper than the PSF resolution of the system and is probably a chance subtraction artifact. The Silber et al. artifact may also be a subtraction residual or polarizer ghost. The second feature looks very much like the “spur” seen extending from the secondary arc in the ACS images.

The MDG02 NICMOS F110W ( $\sim J$ ), F160W ( $\sim H$ ), and F205W ( $\sim K$ ) images have considerably poorer sampling than those from ACS ( $0''.076$  vs.  $0''.025$  pixel $^{-1}$ ). The F205W image was taken at a non-optimal focus position and so is ignored. The residuals from the diffraction spikes, which appear  $2 \times$  wider at  $H$  than  $I$ , block large portions of the ring including the “gap”, “depression”, and secondary arc. The two “gaplets” are visible, however. The front/back amplitude ratios are  $\sim 4$  for both filters, compared to 3.3 for ACS  $I$ . To measure the integrated ring fluxes, they replaced the blocked pixels of the ring with the mean disk flux per pixel. Their integrated F/B ratios are  $1.41 \pm 0.03$  ( $J$ ) and  $1.39 \pm 0.02$

( $H$ ), compared with 1.31 for ACS  $I$ . These images were taken only 14 days after those from WFPC2, but the WFPC2 F/B ratio is considerably higher (1.56 – 1.80, depending on the study). How much of this difference can be attributed to the longer wavelength is unknown, but this may be evidence for short-period ring illumination variations.

The Keck 3.8  $\mu\text{m}$  ( $L'$ ) image (D) has some significant differences in comparison with those at shorter wavelengths. The distance between the binary's center of mass and the forward edge of the ring is  $0''.1$  greater than in the  $HST$  images. D04 attribute this to the decreased opacity at longer wavelengths of the dust along the inner forward edge. The “gap” is seen, though at reduced contrast relative to the other  $HST$  and ground-based images, perhaps indicating a reduction in the extinction caused by the shadowing circumstellar material. There are no signs of the “gaplets.” The eastern side is well defined in  $L'$ , while it is ambiguous in ACS  $I$ . This may also point to reduced extinction. The southeast quadrant is the faintest section in the Keck image, being within the noise; in ACS, this section is brighter than the eastern extreme, which contains the “depression.” There is no indication of the “secondary arc” above the level of the residuals near the stars.

The most significant feature of the Keck  $L'$  image is the unexpectedly large amount of forward scattering. The F/B amplitude ratio is  $> 5$  and the integrated F/B ratio is  $\sim 2.5$ , well above that seen in any of the shorter wavelength images. A single ISM-like grain size distribution would cause scattering to become more isotropic at longer wavelengths, in which case the  $L'$  image should show little forward scattering, extrapolating from the shorter wavelengths. D04 suggest that Keck is seeing larger ( $> 1\mu\text{m}$ ) particles that are not visible at shorter wavelengths, thus explaining the increased forward scattering. These larger particles are located closer to the disk midplane ( $\sim 25$  AU versus  $\sim 50$  AU at shorter wavelengths) and so could only be seen at longer wavelengths that could penetrate through the thick dust. That the  $L'$  image is seeing further into the disk is evident by the increase in the separation of the forward ring edge and the stars. D04 suggest that this vertical stratification of particle sizes relative to the disk height is evidence for grain growth close to the disk midplane, where particles have a greater chance of colliding and coagulating.

#### 4.4. Shadows and Warping

The variations along the ring suggest that the illuminated surface of the disk is irregular. They include:

- The intensity distribution along the forward edge is asymmetric about the line of sight.
- The forward side appears to vary in brightness over time.

- The western side contains a series of likely azimuthal shadows (the “gap” and “gaplets”).
- The western side of the ring is brighter, narrower, and has a sharper (though irregular) inner edge than the eastern side.
- The extreme eastern inner edge has a lower intensity and the outer edge contains narrow filaments.

The first three of these can be easily explained by shadowing caused by optically thick (or nearly so) concentrations of dust between the stars and the disk. The asymmetry in the forward edge could be altered by material very near one of the stars, perhaps associated with the secondary arc. Orbital motion of the material or the star could then change the distribution of light along the forward surface over a matter of hours or days.

The gaps along the western side are almost certainly shadows. There is no sign of a depletion of material in the gap in the millimeter images (Guilloteau, Dutrey, & Simon 1999). Given the viscosity of the massive, gas-rich disk, it is likely that any resonantly-created gap would be filled in quickly. The shadowing material must be fairly dense, though, to cause the most prominent gap to appear even at  $\lambda = 3.8\mu\text{m}$ .

The last two items in the list are more difficult to explain with only shadowing, and they imply that the ring is intrinsically asymmetrical. Guilloteau, Dutrey, & Simon (1999) noted that their mm continuum image shows an apparent density enhancement along the western side, which the scattered light images show is brighter than the opposite side. If this enhancement is real, then it may indicate that the density distribution of scatterers is also different around the ring. An azimuthal dependence of the disk flaring or scale height would alter both the scattering phase angle and the projected surface area. A change in the flaring function could explain why the east side appears wide and poorly-defined along its inner edge while the west side is bright, narrow, and has a well-defined edge. It could also explain the asymmetry along the forward edge. However, the timescale for density distribution variations is too long to cause the illumination changes seen between the ACS and WFPC2 images.

Variations in the density distribution would not be surprising, given the strong tidal influence of the binary. Most circumbinary disk models (Artymowicz & Lubow 1996) show density asymmetries caused by the orbital eccentricity of the binary, including spiral patterns. These could cause the scattering surface of the disk to be highly variable on small spatial scales, in effect creating localized flared or self-shadowing regions. Perhaps this is an explanation for the filaments.

#### 4.5. Ring Color

The ring has a significant red excess in the visible ( $V - I_c = 0.8$ ) while the near-IR colors are more neutral ( $J - H = 0.1$  and  $H - K = -0.04$ ; MDG02). The easiest explanation for this is that increasing extinction from circumstellar material accounts for the lower  $F_{ring}/F_{stars}$  flux ratio towards shorter wavelengths. KSW02 derived a required extinction of  $A_v = 1.2$  mag. This simple solution, however, ignores any color effects caused by the wavelength-dependent scattering properties of the ring material itself.

Wood et al. (1999) reported the first results of matching multiple scattering models of GG Tau to multi-color data (the  $J$ ,  $H$ , and  $K$  band images of R96), assuming grain properties that reproduce the ISM extinction curve. Their models resulted in a blue, rather than red, color excess, even when extinction by a circumstellar disk was added to match  $F_{ring}/F_{stars}$ . MDG02 later computed models to match their NICMOS images. Using a somewhat similar disk geometry but different grain properties (though still matching the ISM extinction curve), they were able to produce a significant red excess without extinction by any circumstellar material. However, their models differ from their NICMOS data by significant amounts in terms of  $F_{ring}/F_{stars}$  and F/B ratios. Their results suggest that uncertainties in grain properties (i.e. scattering phase function, albedo, and size distribution) may be the primary source of color mismatches between models and observations, rather than geometrical or possible circumstellar extinction effects.

#### 4.6. Ring Variations and Modeling

D04 have expanded on the work of MDG02 to include models for the WFPC2  $I$  band and Keck  $L'$  images in addition to those from NICMOS. Rather than simply matching the integrated F/B ratios, they attempted to find models whose azimuthal brightness profiles best matched the observed ones. They claim that this provides a more accurate indication of the grain scattering properties than does the simple F/B contrast ratio. As previously discussed, they were unable to match the azimuthal profiles at all wavelengths with a single grain size distribution, requiring instead a separate distribution of larger grains in order to explain the large amount of forward scattering at  $L'$ . Their models, however, are incomplete as they significantly underestimate the F/B contrast and overestimate the  $F_{ring}/F_{stars}$  ratio at every wavelength (they do suggest  $A_v = 1$  mag of extinction between the stars and ring to reduce the ratio). So far, no one has developed a model that simultaneously reproduces the ring's color, forward/backside contrast, and ring-to-stars flux ratio.

The apparent position-and-time-dependent variability in the illumination pattern on the

ring may create difficulties for those modeling the dust distribution and grain properties of the GG Tau disk using non-contemporaneous datasets, especially when comparing images at multiple wavelengths. The forward/backside contrast is the strongest constraint on the scattering phase function, and it is now evident that this value can vary over time within the same passband. Time-resolved imaging of the GG Tau ring is required to verify the illumination variations and establish the variation timescale. This may be possible in the future with further improvements to ground-based adaptive optics or in the present with additional *HST* observations.

The need obviously exists for integrated modeling that produces a dynamical simulation of the disk and then shows how it would appear in scattered light for a series of assumed grain and initial dust and gas distributions. Such models could indicate how much asymmetry would be expected from disk surface warping.

## 5. Conclusions

We have presented *HST/ACS* *V* and *I* band images of the GG Tau binary system and its disk taken in 2002. They confirm the existence of material near the secondary component, filamentary or spiral structure along the eastern side of the ring along with a broad region of low surface brightness (the “depression”), and the “gap” in the west as well as less prominent gaps toward the northwest. The *V* image unambiguously shows for the first time the far side of the circumbinary ring. The ring is redder than the apparent light from the stars with  $\Delta V - I_c = 0.81$ . There are no significant color variations within the disk. The forward edge of the ring in the 1997 WFPC2 *I* image was  $\sim 20\%$  brighter than it was in the ACS exposure, indicating a time-variable illumination pattern.

The gaps indicate that there is circumstellar material that creates shadows on the circumbinary disk. The asymmetries in the ring suggest that the illuminated disk surface may also be warped due to tidal interactions with the binary. There is a need for scattered light models using dust density distributions derived from dynamical simulation of systems similar to GG Tau. The models need not exactly match the observed images, but rather indicate how warping of the disk may affect its appearance, placing some constraints on what features may be due to illumination or structural variations. The apparent time variation in the illumination pattern further complicates the analyses, especially when comparing images at multiple wavelengths taken at different epochs. Monitoring of GG Tau on short and long timescales is needed.

## 6. Acknowledgements

ACS was developed under NASA contract NAS 5-32865. This research was supported by the ACS Science Team under NASA grant NAG5-7697. The authors thank F. Ménard and C. McCabe for discussions concerning these and previous results, and the reviewer for many useful suggestions.

## REFERENCES

Artymowicz, P. & Lubow, S. H. 1996, *ApJ*, 467, L77

Close, L. M. et al. 1998, *ApJ*, 499, 883

Duchêne, G., McCabe, C., Ghez, A. M., & Macintosh, B. A. 2004, *ApJ*, 606, 969

Dutrey, A., Guilloteau, S., & Simon, M. 1994, *A&A*, 286, 149

Guilloteau, S., Dutrey, A., & Simon, M. 1999, *A&A*, 348, 570

Hartigan, P. & Kenyon, S. J. 2003, *ApJ*, 583, 334

Itoh, Y. et al. 2002, *PASJ*, 54, 963

Krist, J. E., Stapelfeldt, K. R., & Watson, A. M. 2002, *ApJ*, 570, 785

Lightfoot, J. F. 1989, *MNRAS*, 239, 665

McCabe, C., Duchêne, G., & Ghez, A. M. 2002, *ApJ*, 575, 974

Pavlovsky, C., et al. 2004, ACS Data Handbook Version 3.0 (STScI)

Roddier, C., Roddier, F., Northcott, M. J., Graves, J. E., & Jim, K. 1996, *ApJ*, 463, 326

Silber, J., Gledhill, T., Duchêne, G., & Ménard, F. 2000, *ApJ*, 536, L89

Sirianni, M., et al. 1998, *Proc. SPIE*, 3355, 608

Stapelfeldt, K. R., Krist, J. E., Menard, F., Bouvier, J., Padgett, D. L., & Burrows, C. J. 1998, *ApJ*, 502, L65

Stapelfeldt, K. R., et al. 1999, *ApJ*, 516, L95

Tamazian, V. S., Docobo, J. A., White, R. J., & Woitas, J. 2002, *ApJ*, 578, 925

Wood, K., Crosas, M., & Ghez, A. 1999, ApJ, 516, 335